

GCRPNet: Graph-Enhanced Contextual and Regional Perception Network for Salient Object Detection in Optical Remote Sensing Images

Mengyu Ren[†], Yutong Li[†], Hua Li^{*}, *Member, IEEE*, Runmin Cong, *Senior Member, IEEE*, Sam Kwong, *Fellow, IEEE*

Abstract—Salient object detection (SOD) in optical remote sensing images (ORSIs) faces numerous challenges, including significant variations in target scales and low contrast between targets and the background. Existing methods based on vision transformers (ViTs) and convolutional neural networks (CNNs) architectures aim to leverage both global and local features, but the difficulty in effectively integrating these heterogeneous features limits their overall performance. To overcome these limitations, we propose a graph-enhanced contextual and regional perception network (GCRPNet), which builds upon the Mamba architecture to simultaneously capture long-range dependencies and enhance regional feature representation. Specifically, we employ the visual state space (VSS) encoder to extract multi-scale features. To further achieve deep guidance and enhancement of these features, we first design a difference-similarity guided hierarchical graph attention module (DS-HGAM). This module strengthens cross-layer interaction capabilities between features of different scales while enhancing the model’s structural perception, allowing it to distinguish between foreground and background more effectively. Then, we design the LEVSS block as the decoder of GCRPNet. This module integrates our proposed adaptive scanning strategy and multi-granularity collaborative attention enhancement module (MCAEM). It performs adaptive patch scanning on feature maps processed via multi-scale convolutions, thereby capturing rich local region information and enhancing Mamba’s local modeling capability. Extensive experimental results demonstrate that the proposed model achieves state-of-the-art performance, validating its effectiveness and superiority.

Index Terms—Optical remote sensing images, salient object detection, visual state space model

I. INTRODUCTION

SALIENT Object detection (SOD) is a fundamental task in the field of computer vision, aiming to identify and segment the most attention-grabbing objects or regions within a scene [1], [2]. As a key prerequisite visual task, research in SOD has been widely applied to areas such as object tracking [3], [4], image segmentation [5], [6], and quality assessment [7], [8]. Traditionally, SOD methods have primarily focused on natural scene images and have achieved remarkable results in

[†] equal contribution, ^{*} corresponding author.

Mengyu Ren and Hua Li are with the School of Computer Science and Technology, Hainan University, Haikou, 570228 China.

Yutong Li is with the School of Information and Communication Engineering, Hainan University, Haikou, 570228 China.

Runmin Cong is with the School of Control Science and Engineering, Shandong University, Jinan, 250061 China.

Sam Kwong is with the School of Data Science, Lingnan University, Hong Kong, China.

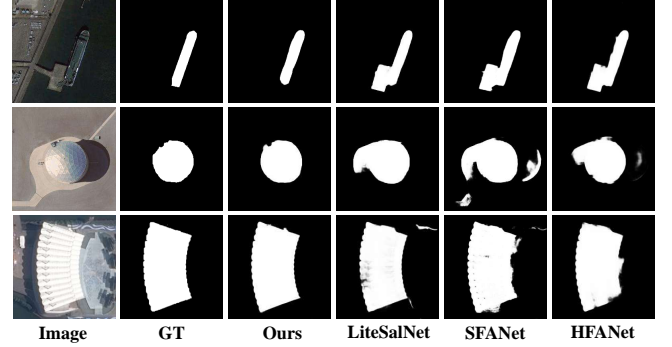


Fig. 1: A simple comparison of GCRPNet and other state-of-the-art methods. LiteSalNet [9] and SFANet [10], employing CNNs architectures, produce inaccurate segmentation due to the lack of global context. HFANet [11] adopts a hybrid architecture, but suffers from performance degradation in detection due to the difficulty in integrating the heterogeneous features from CNNs and ViTs.

that domain. In recent years, with the continuous advancement of satellite remote sensing technology, salient object detection in optical remote sensing images has increasingly attracted the attention of researchers. Compared with natural images, optical remote sensing images pose numerous challenges for salient object detection, such as low target-background contrast, significant variations in target scale, and complex object structures. These factors make it difficult for many SOD methods that perform well on natural images to be directly transferred to remote sensing scenarios. As a result, researchers have developed specialized models tailored to the characteristics of remote sensing images, aiming to effectively detect salient objects in optical remote sensing imagery.

Traditional optical remote sensing image salient object detection (ORSI-SOD) methods [12]–[17], typically rely on color priors and handcrafted features such as positional cues and spatial structures to identify salient objects. However, due to their lack of learnability, these methods struggle to adapt to the complex and variable nature of remote sensing scenes, which limits their performance.

Deep learning-based ORSI-SOD methods has achieved significant progress over the past decade. The introduction of convolutional neural networks (CNNs) and visual transformers (ViTs), has substantially enhanced the performance of

ORSI-SOD models. CNNs, with their local receptive fields, offer high computational efficiency and strong adaptability to scale variations, making them widely adopted in ORSI-SOD tasks. For instance, SFANet [10] enhances multiscale semantic representation through progressive flow and uncertainty-aware refinement. LiteSalNet [9] focuses on efficiency by combining lightweight attention modules with a multistream decoder for accurate saliency detection. Nevertheless, due to the local sliding window operations inherent in CNNs, these methods often lack the ability to model global semantic dependencies. As depicted in LiteSalNet [9] and SFANet [10] from Fig.1, this limitation may lead to segmentation errors and imprecise boundaries, especially when dealing with remote sensing images that contain low-contrast and large-sized objects.

To address this issue, researchers have introduced ViTs into ORSI-SOD tasks to enhance the model’s capacity for global information modeling. ViTs leverage self-attention mechanisms to perform global modeling, effectively compensating for CNNs’ limited receptive field. Their strong global modeling ability makes them particularly advantageous in segmentation tasks involving complex remote sensing imagery. For example, *Gao et al.* [18] introduced a novel adaptive spatial tokenization Transformer framework that produces high-quality saliency maps. Meanwhile, HFANet [11] integrates a hybrid encoder that combines CNN and Transformer to obtain features containing both global semantic relationships and local spatial details, enabling accurate detection of salient objects in complex backgrounds. However, ViTs lack local inductive bias in modeling spatial structures [19], [20], making it difficult to represent fine-grained object details and often resulting in blurred segmentation boundaries. In hybrid architectures [11], [21], [22], theoretically the local detail modeling of CNNs and the global relational representation of ViTs should be complementary. However, relevant studies [23]–[25] have shown that simply combining the two fails to achieve the expected synergistic benefits. This is mainly due to significant differences in their feature representation, receptive field mechanisms, and output paradigm. As depicted in HFANet [11] from Fig.1, these disparities lead to semantic inconsistencies and fusion noise, which in turn hinder effective integration and ultimately degrade overall model performance.

To effectively address the aforementioned challenges, we propose a novel network architecture named graph-enhanced contextual and regional perception network (GCRPNet), which is specifically designed to tackle issues such as low object-background contrast and large variations in object scales, among other issues, in ORSI-SOD tasks. Built upon the conventional encoder-decoder architecture, GCRPNet employs Mamba model [26], [27] as its core modeling backbone. The primary motivation lies in the fact that Mamba employs a selective scanning algorithm to capture long-range dependencies while possessing good stability and scalability, which makes it possible to achieve an effective modeling balance between global context and local region details. To address the challenges of blurred object boundaries and low contrast between salient objects and backgrounds in ORSIs, we propose a difference-similarity guided hierarchical graph attention module (DS-HGAM). This module integrates multi-

scale features at skip connections and utilizes a graph neural network [28] to model the spatial relationships and contextual dependencies among the fused features. In this way, our model can better learn the structural differences between foreground and background, thereby reducing segmentation errors caused by boundary ambiguity. Meanwhile, to handle the problem of multi-scale object variations and mitigate the disruption of local region structures caused by Mamba’s scanning process to enhance its local modeling capability, we introduce a locally enhanced visual state space (LEVSS) module. This module first feeds features into a multi-granularity collaborative attention enhancement module (MCAEM) to extract multi-scale local information. It is then followed by a locally enhanced 2D selective scan (LESS2D) operation. Unlike traditional scanning strategies, LESS2D adaptively partitions the feature maps into blocks based on spatial resolution, and performs directional scanning within each block to model the dependencies among local pixels. This method not only strengthens the model’s ability to represent multi-scale features, enhancing its adaptability to scale-diverse targets in ORSIs, but also through a process of block partitioning, directional scanning, and integration, enables the model to enhance local region feature representation while simultaneously achieving global contextual modeling. This improvement in local detail modeling capability further boosts the model’s segmentation accuracy in complex scenes. We conduct extensive comparative experiments on two widely used benchmark datasets (i.e., ORRSd [29] and EORRSd [30]), and the results demonstrate that GCRPNet significantly outperforms existing state-of-the-art methods on the ORSI-SOD task. Our main contributions can be summarized as follows:

- 1) We propose a novel network architecture named GCRPNet, which enhances local region feature representation while achieving global context modeling, and introduces a graph-enhanced module to strengthen multi-scale interactions and boundary modeling, thereby significantly improving the detection accuracy of ORSI-SOD.
- 2) We introduce the DS-HGAM, which leverages a graph attention mechanism to model spatial relationships and contextual dependencies across the fused multiscale features, thus enhancing the model’s structural perception capability and enabling it to effectively learn the differences between foreground and background.
- 3) We propose LEVSS, a module that integrates our proposed MCAEM and LESS2D. It enhances the model’s capability in modeling local region details and effectively combines global context modeling with local feature learning, thereby significantly improving the accuracy and robustness of feature representation.
- 4) Experimental results on two ORSI-SOD benchmark datasets demonstrate that our proposed method outperforms existing state-of-the-art approaches.

II. RELATED WORK

A. NSI-SOD

Early SOD methods primarily relied on hand-crafted low-level features and heuristic priors, such as color contrast [15],

boundary connectivity [16], and the center-surround assumption. These approaches could achieve reasonable performance in simple backgrounds, but their effectiveness was often limited in complex scenes or multi-object backgrounds due to a lack of semantic understanding of image content. In recent years, deep learning-based SOD methods have gradually become the mainstream [31]. These methods typically adopt end-to-end network architectures that automatically learn saliency representations from large-scale annotated datasets, leading to significant improvements in detection accuracy and fine-grained performance.

CNNs have achieved remarkable progress in the field of SOD due to their powerful multi-level feature learning capabilities. *Li et al.* [32] significantly improved visual saliency detection performance by leveraging multi-scale features extracted from deep convolutional networks, combined with spatial consistency enhancement and multi-level image segmentation fusion techniques. *Sun et al.* [33] proposed a novel U-shaped network architecture that effectively integrates multi-scale features and edge information to address issues such as boundary blurring and inaccurate localization commonly found in existing methods. *Zhao et al.* [34] simultaneously modeled salient object and salient edge information, using edge cues to guide the fusion of salient object features, thereby achieving more accurate localization and boundary detection. With their superior global modeling capabilities and ability to capture long-range dependencies, Transformer-based models have been increasingly applied to NSI-SOD tasks. *Liu et al.* [35] proposed a pure Transformer-based architecture, rethinking the SOD task from a sequence-to-sequence perspective and enhancing detection performance by modeling global long-range dependencies. *Zhang et al.* [36] introduced a novel framework based on generative visual Transformers, incorporating latent variables and an energy-based prior distribution to generate uncertainty maps that align with human perception, significantly improving detection performance. *Liu et al.* [37] proposed TriTransNet, which reconsiders the RGB-D SOD task from the perspective of multi-scale feature fusion. By modeling long-range dependencies across hierarchical features and enhancing RGB representations with depth information, the model achieves more accurate salient object localization and boundary delineation. Recently, Mamba has gained attention in the SOD field due to its strong ability to model long-range dependencies. *Zhang et al.* [38] introduced a Mamba-based dual-stream feature extractor and a cross-modal fusion module to effectively integrate RGB and depth information, improving salient object detection performance. *He et al.* [39] proposed a novel unified framework named Samba based on the Mamba architecture, achieving excellent performance and low computational cost across various SOD tasks.

B. ORSI-SOD

Although SOD has achieved significant progress on natural scene images (NSIs), directly applying existing methods to ORSIs still faces numerous challenges. NSI-SOD methods are primarily designed for natural scenes from a ground-level perspective, typically relying on clear object boundaries, rich

textures, and prominent semantic context. However, objects in RSIs often exhibit characteristics such as small size, low contrast, minimal inter-class variance, and strong background interference, making it difficult for existing NSI-based methods to generalize effectively in remote sensing scenarios. To address these issues, a series of SOD approaches specifically tailored for ORSIs—referred to as ORSI-SOD—have emerged in recent years, aiming to enhance detection performance in complex remote sensing environments.

Thanks to their powerful semantic representation and local feature extraction capabilities, CNNs can accurately capture fine-grained local features in ORSIs. In recent years, many CNN-based ORSI-SOD models have achieved notable progress. LV-Net [29] leverages a dual-stream pyramid module and a nested encoder-decoder structure to effectively handle the multi-scale and complex background challenges in ORSIs. DAFNet [30] transmits low-level attention cues to deeper layers to generate accurate high-level attention maps, effectively suppressing background noise and highlighting salient objects. ACCoNet [40] enhances saliency detection by coordinating adjacent features and capturing contextual information, leading to more comprehensive activation of salient regions. MCP-Net [41] introduces a memory module to utilize both inter-image and intra-image contextual information, significantly improving the detection performance for salient objects in optical RSIs. Similarly, Transformer-based methods have been increasingly applied to ORSI-SOD tasks, aiming to overcome the limitations of CNNs in handling complex backgrounds, multi-scale targets, and weak object boundaries in optical remote sensing images. TLCKD-Net [42] adopts a Transformer-based encoder to effectively capture global features, addressing traditional methods' shortcomings in handling complex backgrounds and salient objects of varying scales and shapes. GeleNet [43] adopts a global-to-local paradigm based on Transformers, combining global feature extraction with local enhancement modules to more precisely locate salient objects and highlight details. However, pure ViT architectures are limited in modeling local information, while targets in optical remote sensing images often exhibit multi-scale and complex shapes, which can easily lead to imprecise boundary segmentation. To address this issue, researchers have proposed hybrid architectures. ASNet [21] integrates Transformer and CNN techniques through a dual-branch encoder that captures both global dependencies and local detail features, adapting to the complexity of RSIs and improving detection performance. ADSTNet [22] combines the strengths of CNNs and Transformers to effectively compensate for global and local information, with boundary-guided modules further assisting in accurate detection and localization.

C. Scanning Mechanism in Visual Mamba

Recently, the emergence of state space models (SSMs) [44], [45] has provided a novel paradigm for global modeling, particularly with the introduction of the Mamba [26] model. Mamba enhances global modeling capability by introducing a selective scanning mechanism and adopts a parallel scanning strategy to effectively capture comprehensive contextual information across the image, facilitating better representation of

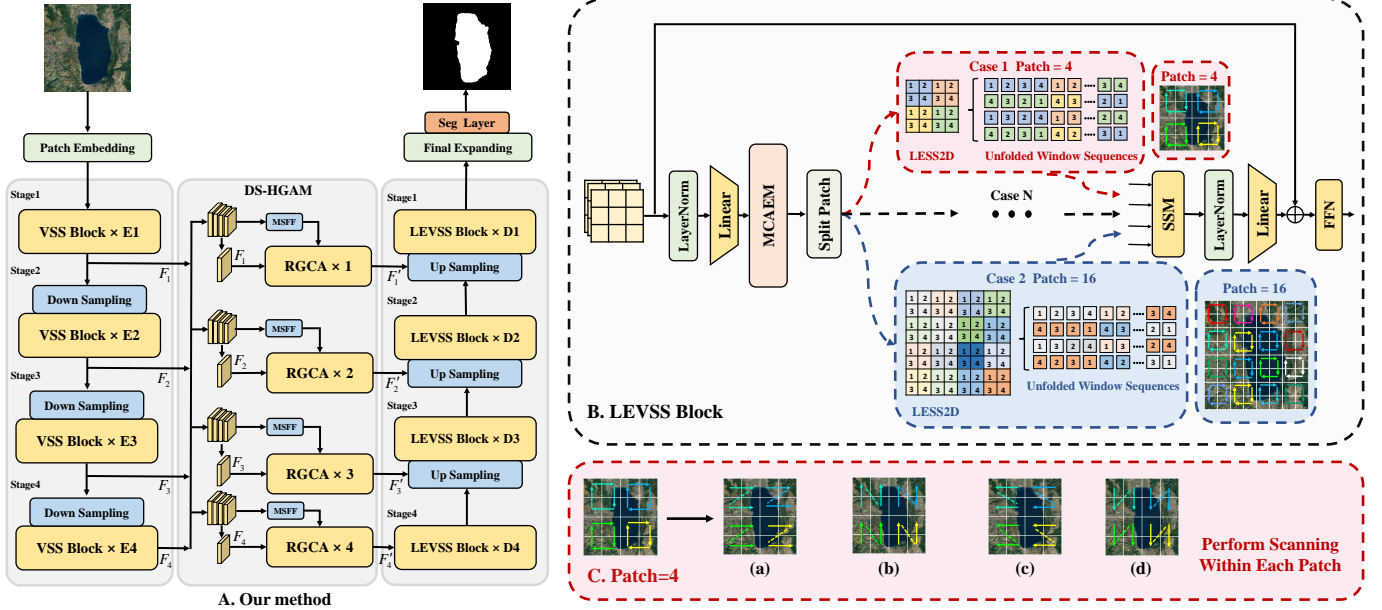


Fig. 2: **Pipeline of the proposed method.** **A:** GCRPNet adopts a U-shaped encoder-decoder architecture. The encoder is built upon the visual state space (VSS) of VMamba. In the skip connections, a DS-HGAM module is employed to enhance the model’s representation capability through feature fusion and a graph attention mechanism. Subsequently, in the decoding stage, the features processed by DS-HGAM are fed into the LEVSS blocks for decoding. **B:** The proposed LEVSS blocks enhance the model’s ability to capture local information through a MCAEM and a LESS2D, aiming for more precise boundary representation. **C:** LESS2D performs four-directional scanning within each image patch.

long-range dependencies. Building on this foundation, Mamba has rapidly advanced in the field of computer vision, giving rise to a variety of visual Mamba architectures [46]–[48]. Despite Mamba’s impressive potential in vision applications, it still faces challenges in local modeling. In current visual Mamba models [27], [46], [49], a common practice is to divide 2D feature maps into patches and scan them into 1D sequences before feeding them into the SSMs for processing. However, images inherently lack a sequential structure, and this serialization conflicts with the spatial locality of image data. As a result, the dependency relationships between neighboring pixels are disrupted, leading to insufficient modeling of fine-grained structures such as edges and textures. This ultimately hinders the SSMs from generating high-quality visual features.

As a crucial component of Mamba architectures in the vision domain, efficient scanning mechanisms play a key role in improving model performance and have become a focal point of current Mamba-related research. Vision Mamba employs a bidirectional scanning mechanism to simultaneously process forward and backward information. VMamba [46] introduces a cross-scanning mechanism that scans images along four different paths to enable more comprehensive feature extraction, and has seen widespread adoption. The Hilbert scanning strategy [50] integrates multiple scanning methods and directions, allowing it to capture local feature information from various angles. The LocalMamba [51] model incorporates a local scanning strategy by dividing the image into multiple non-overlapping local windows, with pixels in each window scanned independently.

III. METHODOLOGY

In this section, we propose a novel architecture named GCRPNet, whose overall structure is illustrated in Fig.2. GCRPNet adopts a typical encoder-decoder framework and integrates three innovative modules: DS-HGAM, MGAM, and LESS2D. To clearly present our work, we first provide a summary and review of existing SSM methods in Section III-A. Then, we introduce the overall architecture of GCRPNet, followed by detailed descriptions of the three core modules, including their design principles and implementation details. Finally, we explain the loss functions used in our approach.

A. Preliminaries

State Space Model: State space model (SSM) [44], [45] such as S4 [52] and Mamba [26] are structured sequence architectures that are inspired by recurrent neural networks (RNNs) and CNNs and have the ability to scale linearly or nearly linearly with sequence length. These models originate from continuous systems, mapping an input sequence $x(t) \in \mathbb{R}^L$ to an output sequence $y(t) \in \mathbb{R}^L$ through a hidden state $h(t) \in \mathbb{R}^N$. More specifically, SSMs are described by the following continuous-time ordinary differential equations (ODEs):

$$h'(t) = \mathbf{A}h(t) + \mathbf{B}x(t) \quad (1)$$

$$y(t) = \mathbf{C}h(t) \quad (2)$$

Where $h(t)$ is the current hidden state, $h'(t)$ is the updated hidden state, $x(t)$ is the current input, $y(t)$ is the output. $\mathbf{A} \in \mathbb{R}^{N \times N}$ is SSM’s evolution matrix, and $\mathbf{B} \in \mathbb{R}^{N \times 1}$, $\mathbf{C} \in \mathbb{R}^{1 \times N}$ are the input and output projection matrices, respectively.

Discrete State Space Models: To integrate continuous-time SSMs into deep models, they need to be discretized. This involves transforming the continuous-time functions into discrete-time sequence-to-sequence mappings. For example, this is seen in models such as S4 [52] and Mamba [26]. One common method is zero-order hold (ZOH). It introduces a time scale parameter Δ , which converts the continuous parameters \mathbf{A} and \mathbf{B} into their discrete versions $\bar{\mathbf{A}}$, $\bar{\mathbf{B}}$.

$$\bar{\mathbf{A}} = \exp(\Delta\mathbf{A}) \quad (3)$$

$$\bar{\mathbf{B}} = (\Delta\mathbf{A})^{-1}(\exp(\Delta\mathbf{A}) - \mathbf{I}) \cdot \Delta\mathbf{B}, \quad (4)$$

$$h_t = \bar{\mathbf{A}}h_{t-1} + \bar{\mathbf{B}}x_t \quad (5)$$

$$y_t = \mathbf{C}h_t \quad (6)$$

B. Overall Structure

The overall structure of GCRPNet, illustrated in Fig.2 (A), the overall architecture of GCRPNet adopts a U-shaped design and consists of three main components: (1) A four-stage VSS encoder built on the VMamba backbone, responsible for multi-scale feature extraction; (2) Four difference-similarity guided hierarchical graph attention module (DS-HGAM) embedded in the skip connections, which fuse the multi-scale features from the encoder and apply graph attention mechanisms to model them; (3) A four-stage locally enhanced VSS (LEVSS) decoder, designed to enhance local modeling and progressively decode the features to obtain fine-grained segmentation maps. In the encoder stage, the input image $I \in \mathbb{R}^{H \times W \times 3}$ first passes through a patch embedding module composed of two convolutional layers, which performs patch-wise embedding. Each encoder stage $s \in \{1, 2, 3, 4\}$ contains a $2 \times$ down-sampling layer followed by multiple stacked VSS blocks for extracting multi-scale features F_i where $i \in \{1, 2, 3, 4\}$. After the encoder, the features from the four stages are fed into the difference-similarity guided hierarchical graph attention module (DS-HGAM) in a cascaded manner. These modules process multi-scale features and integrate them into their respective feature representations. Through the graph attention mechanism, the feature F_i^g is obtained, which captures long-range relationships among pixels in the fused feature maps, thereby enabling the model to identify salient objects in the presence of severe background interference and enhance its discriminative capability for salient regions. In the decoder, the network comprises four decoding stages, each stage D_s , where $s \in \{4, 3, 2, 1\}$ incorporates multiple stacked LEVSS blocks to enhance local feature modeling capability. The first decoding stage D_4 directly takes the skip-connected features F_4^g from the encoder as input. The remaining three stages $s \in \{3, 2, 1\}$ concatenate high-level skip-connected features F_s^g with the upsampled intermediate features from the previous stage along the channel dimension to form the fused input features.

C. Difference-Similarity Guided Hierarchical Graph Attention Module

Traditional skip connections in U-shaped network architectures, due to their simplistic and direct feature concatenation

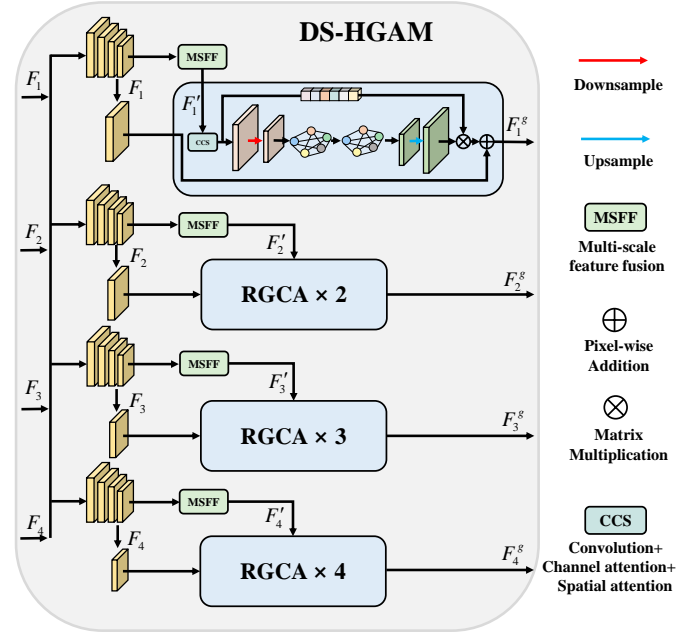


Fig. 3: Illustration of DS-HGAM

strategy, which lack modeling of spatial context and fine-grained details, often fail to effectively distinguish foreground from background in low-contrast scenarios, leading to blurred boundaries and inaccurate localization. Notably, although OR-SIs suffer from complex backgrounds and low contrast, salient objects often exhibit a clustered distribution with similar visual patterns across regions. To better exploit this property, we propose a DS-HGAM. Instead of directly concatenating encoder and decoder features, DS-HGAM performs multi-scale fusion of skip-connected features and employs a graph neural network to model spatial relationships and contextual dependencies across hierarchical levels. By computing attention across regions and scales, DS-HGAM effectively captures complementary information among visually similar patches at different resolutions. This not only enhances the model's structural perception capability but also strengthens the representation of fine-grained details, enabling more accurate saliency prediction in low-contrast and cluttered scenes.

Specifically, DS-HGAM (as illustrated in Fig.3) first targets the four groups of skip-connected features F_i , where $i \in \{1, 2, 3, 4\}$ from different encoding layers and introduces multi-scale feature fusion (MSFF) modules for each. These modules perform spatial alignment on the multi-scale features, fusing them into features of corresponding resolutions. The feature fusion process is as follows:

$$F_i^g = Conv_{1 \times 1}(Concat(\phi_1(F_1), \phi_2(F_2), \phi_3(F_3), \phi_4(F_4))) \quad (7)$$

Where $\phi_i(\cdot)$ denotes the operation of adjusting features to the resolution of the i layer via upsampling or downsampling; $Concat$ represents channel-wise concatenation; $Conv_{1 \times 1}$ denotes a convolution operation used to compress the number of channels after concatenation.

Subsequently, the RGCA module takes the fused feature F_i' as input, where $i \in \{1, 2, 3, 4\}$. Feature F_i' is first fed into the CCS module. The CCS module combines channel attention and spatial attention to enhance the focus on salient regions within the target, followed by convolution operations to process the fused features and enhance their representational power.

$$F_i^c = CCS(F_i') \quad (8)$$

Meanwhile, to reduce the number of parameters processed by the subsequent graph attention networks operations, the RGCA module downsamples the fused feature, the feature $F_i^c \in \mathbb{R}^{h \times w \times c}$ is fed into a convolutional layer with a kernel size of $s \times s$ and a stride of s . Then, each row of pixels in the output feature $F_i^{c'} \in \mathbb{R}^{h/s \times w/s \times c}$ is treated as a graph node $f_i \in \mathbb{R}^d$. The graph composed of image patches can be represented as: $F_{in} = \{f_1, f_2, \dots, f_n\}, n = h/s \times w/s$. To transform the input features into higher-level representations and enhance the expressiveness of the network, we apply a shared learnable weight matrix $W \in \mathbb{R}^{d' \times d}$ to linearly transform each node. Then, a shared self-attention weight matrix $l \in \mathbb{R}^{2d' \times 1}$ is used to compute the attention coefficients between node pairs. We only compute a_{ij} for node j , where \mathcal{N}_i denotes the set of first-order neighboring nodes of node i . To better compare the attention coefficients a between different nodes, we apply the softmax function to normalize all the selected j . Therefore, the formula for a_{ij} is:

$$a_{ij} = \frac{\exp(\sigma(l^T [W \vec{f}_i || W \vec{f}_j]))}{\sum_{n \in \mathcal{N}_i} \exp(\sigma(l^T [W \vec{f}_i || W \vec{f}_n]))} \quad (9)$$

Here, T denotes the transpose operation, $||$ represents the concatenation operation, and σ is the LeakyReLU activation function. Assuming δ is the ELU activation function, the final output feature can be expressed as:

$$\vec{f}_i' = \delta \left(\sum_{n \in \mathcal{N}_i} a_{ij} W \vec{f}_j \right) \quad (10)$$

The final output feature has the same dimensionality as the input feature, denoted as $F_{out} = \{f_1', f_2', \dots, f_n'\}, f_n' \in \mathbb{R}^d$. This output feature F_{out} is then passed through a deconvolution and upsampling operation, and multiplied with the obtained channel attention weight w to form the residual information flow of F_i , thereby compensating for the information lost during downsampling.

The overall operation process is as follows:

$$F_i^{gat} = GAT(F_i^c) \otimes CA(F_i^c) \quad (11)$$

$$F_i^g = F_i^{gat} + F_i \quad (12)$$

Finally, fuse the original feature F_i with the enhanced feature F_i^{gat} output through a residual connection to produce the refined feature representation F_i^g .

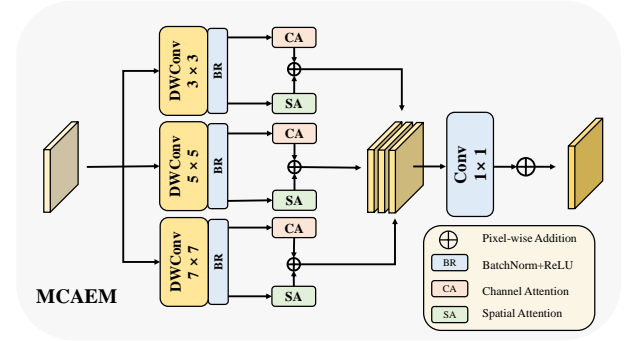


Fig. 4: Illustration of the proposed MCAEM

D. Locally Enhanced Visual State Space

Salient objects in ORSIs often exhibit significant variations in scale and complex structural characteristics. This requires the model to possess strong capabilities in both local region and multi-scale representation in order to achieve accurate saliency detection. However, the traditional Mamba scanning strategy flattens 2D images into 1D sequences, disrupting local region spatial dependencies and making it difficult for the model to capture fine details. How to enable the Mamba model to effectively model local region is still a challenge. Therefore, we propose the LEVSS module, which is designed on top of the original Mamba module to enhance the representation of local region information and significantly improve the model's ability to capture local region dependencies. The structure of LEVSS is illustrated in Fig.2 (B) and consists of two main components: MCAEM and LESS2D.

1) *Multi-Granularity Collaborative Attention Enhancement Module*: In the ORSI-SOD task, effectively adapting to multi-scale object variations is essential for robust saliency detection. To this end, we propose a MCAEM that effectively combines multi-scale feature extraction with channel and spatial attention mechanisms to enhance feature representation (as illustrated in Fig.4). This module is integrated into the LEVSS block and applied before sequence scanning, aiming to reinforce multi-scale feature representation and compensate for the limited local region perception capability of sequence modeling structures.

Specifically, MCAEM employs depthwise separable convolutions [53] with three different kernel sizes ($3 \times 3, 5 \times 5, 7 \times 7$) to extract features at multiple receptive fields, thereby strengthening the representation of structural information across scales. In parallel, channel attention and spatial attention mechanisms are applied to the extracted features for adaptive enhancement. Channel attention adjusts the responses of different semantic types (e.g., edges, textures, colors) from a global perspective, which helps improve detection accuracy. Meanwhile, spatial attention focuses on localizing important regions in the image and emphasizes discriminative areas, while the parallel design helps mitigate redundancy and reduce biased dependencies between feature channels or spatial locations.

Given an input feature map $F_i \in \mathbb{R}^{h \times w \times c}$, the overall processing of MCAEM can be summarized in the following

steps:

$$F'_k = DWConv_{k \times k}(F), k \in \{3, 5, 7\} \quad (13)$$

$$F_k^{att} = CA(F'_k) + SA(F'_k) \quad (14)$$

$$F_{out} = F + Conv_{1 \times 1}(Concat(F_3^{att}, F_5^{att}, F_7^{att})) \quad (15)$$

Here, $CA(\cdot)$ and $SA(\cdot)$ refer to the channel and spatial attention modules respectively, $Conv_{1 \times 1}$ represents a 1×1 convolution, and $Concat$ indicates concatenation along the channel dimension.

2) *Locally Enhanced 2D Selective Scan* : In salient object detection of complex objects, accurately modeling local details plays a vital role in improving detection accuracy. To this end, we propose a LESS2D module, which aims to address the limitations of traditional SS2D in capturing local features, while simultaneously balancing the Mamba model's global context modeling capability with enhanced sensitivity to local details.

Specifically, the core motivation of this module lies in the observation that as the resolution of the feature map increases, its spatial geometric structure becomes more complex, and the contained local details grow richer. Flattening a 2D image into a 1D sequence not only disrupts the original spatial adjacency but also causes local region features to become dispersed in the sequence, thereby weakening the model's ability to capture local dependencies. To address this issue, we propose LESS2D (as illustrated in Fig.2 (B)) and integrate it into a four-stage decoder architecture. Given an input image $I \in \mathbb{R}^{h \times w \times c}$, we perform the split patch operation on the extracted multi-scale feature maps, dividing them into multiple image blocks to facilitate subsequent local feature modeling and processing. In our method, for low-resolution feature maps (e.g., $\frac{1}{16}h \times \frac{1}{16}w$), due to their limited spatial modeling range and concentrated geometric relationships, LESS2D applies a global four-directional scanning strategy to fully retain long-range dependency modeling capability. In contrast, for medium and high resolution feature maps (e.g., $\frac{1}{8}h \times \frac{1}{8}w$, $\frac{1}{4}h \times \frac{1}{4}w$, $\frac{1}{2}h \times \frac{1}{2}w$), the image is divided into multiple non-overlapping local patches (e.g., 4, 16, and 64 patches, respectively), and four-directional scanning is performed independently within each patch. The scanning sequences from all patches are then concatenated in order to form a complete sequence, which is subsequently fed into downstream modules for further processing.

Taking a feature map F of size $\frac{1}{4}h \times \frac{1}{4}w$ as an example, we divide it into 16 non-overlapping sub-regions, each denoted as F_i , where $i \in \{1, 2, \dots, 16\}$. The overall process is carried out as follows:

$$Scan_4(F_i) = [Scan^{\rightarrow}(F_i), Scan^{\downarrow}(F_i), Scan^{\leftarrow}(F_i), Scan^{\uparrow}(F_i)] \quad (16)$$

$$\vec{S} = Concat(Scan^{\rightarrow}(F_1), Scan^{\rightarrow}(F_2), \dots, Scan^{\rightarrow}(F_{16})) \quad (17)$$

Each block contributes four directional scans denoted as $Scan^{\rightarrow}$, $Scan^{\downarrow}$, $Scan^{\leftarrow}$, and $Scan^{\uparrow}$ (as illustrated in Fig.2 (C)), which represent left-to-right, top-to-bottom, right-to-left, and bottom-to-top scanning, respectively. Eq. 17 illustrates the left-to-right scanning process, where \vec{S} represents the complete image sequence.

E. Loss Function

We define an integrated loss function to constrain the entire training process. Our loss function consists of two components: binary cross-entropy (BCE) loss and intersection over union (IoU) loss. Specifically, we calculate the losses for saliency predictions at four different scales: P_1 , P_2 , P_3 , and P_4 , where P_1 is the final saliency map while P_2 , P_3 , and P_4 are intermediate-scale saliency maps are used for auxiliary training. The total loss function is defined as:

$$\mathcal{L}_{total} = \sum_{i=1}^4 \lambda_i (\mathcal{L}_{BCE}(P_i, G_i) + \mathcal{L}_{IoU}(P_i, G_i)) \quad (18)$$

Where λ_i are the weight coefficients, P_i represents the saliency map, and G_i is the corresponding ground truth map. In this paper, we set $\lambda_1 = \lambda_2 = \lambda_3 = \lambda_4$ to ensure that the feature maps at all scales contribute equally to the final loss function.

BCE loss is used to ensure pixel-wise classification accuracy. For each predicted saliency map P_i and its corresponding ground truth map G_i , the binary cross-entropy loss is defined as:

$$\mathcal{L}_{BCE}(P_i, G_i) = -\frac{1}{N} \sum_{j=1}^N [G_i^j \log(P_i^j) + (1 - G_i^j) \log(1 - P_i^j)] \quad (19)$$

Where N represents the total number of pixels, and P_i^j and G_i^j represent the values at the j -th pixel of the predicted map and the ground truth map, respectively. IoU loss is used to maximize the overlap between the predicted region and the ground truth region. The IoU loss is defined as:

$$\mathcal{L}_{IoU}(P_i, G_i) = 1 - \frac{\sum (P_i \odot G_i) + \epsilon}{\sum (P_i + G_i - P_i \odot G_i) + \epsilon} \quad (20)$$

Where \odot denotes element-wise multiplication, and ϵ is a smoothing term used to prevent division by zero errors.

IV. EXPERIMENTS

A. Experimental Setup

1) *Datasets*: To evaluate the effectiveness of the method, we trained and tested it on two public benchmark datasets for ORSI-SOD: ORSSD [29] and EORSSD [30].

The ORSSD dataset is the first publicly released dataset in the field of ORSI-SOD. This dataset contains a total of 800 high-quality visible light remote sensing images, which include eight types of remote sensing objects, such as islands, ships, and vehicles. Of these, 600 images are allocated to training sets for algorithm training and optimization, while the remaining 200 images are designated as test sets to evaluate the model's performance and generalization ability.

The EORSSD dataset is an enhanced version of the ORSSD dataset, featuring significant improvements in both data volume and diversity. Compared to the original ORSSD, the data volume of EORSSD has more than doubled, offering a richer array of training and testing samples. The dataset comprises 2,000 high-resolution images along with corresponding pixel-level ground truth, encompassing both high-resolution satellite images and low-resolution aerial images. It includes nine distinct remote sensing objects: ships, airplanes, cars, buildings,

water, islands, roads, none, and others. Of these, the training set contains 1,400 images, while the test set consists of 600 images.

2) *Implementation Details*: In this study, we implemented the proposed method using the PyTorch framework and conducted all experiments on an RTX 4090Ti GPU. We set the learning rate to $1e-4$, the batch size to 4, and employed the AdamW optimization strategy for training. To ensure consistency in the input data, each image was resized to 384×384 pixels before being fed into the model. Additionally, to effectively mitigate overfitting during training, we introduced a series of data augmentation techniques, including random scaling and cropping, random image transformations, and normalization. Finally, we trained the model for 100 epochs on the ORSSD and EORSSD datasets.

3) *Evaluation Metrics*: To comprehensively evaluate the performance of the proposed method, we adopt eight widely used evaluation metrics to assess the performance of the model. These metrics include the Mean Absolute Error (MAE), S-measure (S_α), F-measure score (F_β), E-measure (E_ξ), adaptive E-measure (E_ξ^{adp}), mean E-measure (E_ξ^{mean}), maximum E-measure (E_ξ^{max}), adaptive F-measure (F_β^{adp}), mean F-measure (F_β^{mean}) and maximum F-measure (F_β^{max}). Specifically, S_α quantifies the structural similarity between the predicted saliency map and the ground truth. F_β is the weighted harmonic mean of precision and recall, where β^2 is set to 0.3 to place greater emphasis on precision over recall. The MAE calculates the average pixel-wise error between the prediction and the ground truth, offering a direct measure of prediction deviation. Furthermore, E_ξ^{adp} , E_ξ^{mean} , and E_ξ^{max} evaluate the E-measure using adaptive thresholding, image-level mean, and maximum values, respectively. These metrics capture structural and distributional consistency from multiple perspectives. Similarly, F_β^{adp} , F_β^{mean} , and F_β^{max} assess the F-measure under the same three thresholding strategies, emphasizing the trade-off between precision and recall.

B. Comparisons With State-of-the-Arts

We compare our method with 15 state-of-the-art methods specifically designed for the ORSI-SOD task, including EMFINet [54], DAFNet [30], ERPNet [55], SBA-Net [56], HFANet [11], ESGNet [57], ACCoNet [40], BSCGNet [58], SFANet [10], RAGRNet [59], UDCNet [60], SOLNet [61], LiteSalNet [9], LGIPNet [62], and DPU-Former [25]. To ensure a fair evaluation, all experiments are conducted under the same conditions on the ORSSD and EORSSD datasets.

1) *Quantitative Comparisons*: The quantitative comparison results between our proposed GCPRNet and other methods are summarized in Tab I. It is evident that our model achieves SOTA performances. On the EORSSD dataset, the quantitative comparison results of our method across eight evaluation metrics are presented at the bottom of the table. It can be observed that our approach achieves the best performance on several key indicators, including F_β^{max} , F_β^{mean} , S_α , and MAE , while also attaining the second-best result on metrics F_β^{adp} , E_ξ^{max} , and E_ξ^{mean} metric. Specifically, compared with the second-best method, our approach achieves performance

gains of 0.82% on F_β^{max} , 0.66% on F_β^{mean} , and 0.85% on S_α , further highlighting its superiority in salient object detection tasks. On the ORSSD dataset, our method also achieves superior performance. Specifically, it attains the best results on five key metrics: F_β^{max} , F_β^{mean} , F_β^{adp} , S_α , and MAE , while also attaining the second-best results on metrics E_ξ^{max} and E_ξ^{mean} . Compared to the second-best method, our approach achieves a 0.93% improvement on metric F_β^{max} , a 0.86% improvement on metric F_β^{mean} , and a 0.83% improvement on metric S_α , while also reducing the MAE by 0.06%, further validating the effectiveness and robustness of our approach.

Figure 5 illustrates the PR and F-measure curves on the ORSSD and EORSSD datasets. Higher curves indicate better performance. Compared with other methods, our approach consistently achieves higher precision and recall. Specifically, our PR curve is closer to the top-right corner, demonstrating superior performance across thresholds. Similarly, our F-measure curve outperforms all competing methods. These results collectively highlight the effectiveness and robustness of our method under various conditions.

2) *Quantitative Comparisons*: Figure 6 presents a qualitative comparison between our model and six of the latest state-of-the-art methods from recent years on the ORSSD and EORSSD datasets. We selected multiple representative ORSI scenarios, including large objects, small objects, elongated structures, and low-contrast objects. Compared with other methods shown in the figure, our model demonstrates superior performance in saliency detection under these complex conditions. For example, in the low-contrast scene in the seventh row, only our model is able to accurately segment the complete contour of the circular building, while other methods suffer from varying degrees of over-segmentation, indicating their limited adaptability to such conditions. This highlights our model’s strong capability in capturing subtle local variations and performing precise boundary localization. Similarly, in the fourth row, which involves small-object detection, our model correctly segments all three yellow objects with clear and non-overlapping boundaries. In contrast, other methods yield blurry and incomplete results, especially for the middle object. These results demonstrate our model’s excellent segmentation ability across different object scales, reflecting its powerful multi-scale feature representation. Moreover, in the l-shaped building scene in the last row, only our method and DPU-Former are able to fully recognize and segment the complete l-shaped structure, while all other methods fail to segment the complete building shape and exhibit obvious segmentation errors. In summary, the qualitative results in Figure 6 comprehensively demonstrate the robustness and accuracy of our proposed model in salient object detection across various complex ORSI scenes. Our approach not only ensures effective global context modeling but also excels at extracting critical local features, enabling the model to learn saliency information more effectively.

C. Ablation Studies

In this section, we conduct comprehensive ablation studies on the EORSSD and ORSSD datasets to demonstrate the

TABLE I: Quantitative comparison results in terms of F_{β}^{max} , F_{β}^{mean} , F_{β}^{adp} , E_{ξ}^{max} , E_{ξ}^{mean} , E_{ξ}^{adp} , S_{α} and MAE score are presented on two benchmark datasets. In the tables, \uparrow and \downarrow indicate that higher and lower values are preferred, respectively. The top three results in each column are highlighted in red, blue, and green, respectively.

Methods	Pubs	EORSSD								ORSSD							
		$F_{\beta}^{max} \uparrow$	$F_{\beta}^{mean} \uparrow$	$F_{\beta}^{adp} \uparrow$	$E_{\xi}^{max} \uparrow$	$E_{\xi}^{mean} \uparrow$	$E_{\xi}^{adp} \uparrow$	$S_{\alpha} \uparrow$	$MAE \downarrow$	$F_{\beta}^{max} \uparrow$	$F_{\beta}^{mean} \uparrow$	$F_{\beta}^{adp} \uparrow$	$E_{\xi}^{max} \uparrow$	$E_{\xi}^{mean} \uparrow$	$E_{\xi}^{adp} \uparrow$	$S_{\alpha} \uparrow$	$MAE \downarrow$
EMFINet	TGRS'21	0.8721	0.8488	0.7987	0.9712	0.9603	0.9502	0.9292	0.0084	0.9002	0.8856	0.8617	0.9737	0.9671	0.9663	0.9366	0.0109
DAFNet	TIP'21	0.8735	0.7982	0.6525	0.9816	0.9382	0.8216	0.9186	0.0053	0.8999	0.8442	0.7565	0.9821	0.9536	0.8928	0.9188	0.0106
ERPNet	TCYB'22	0.8744	0.8272	0.7174	0.9665	0.9364	0.8995	0.9254	0.0082	0.9036	0.8799	0.8392	0.9738	0.9604	0.9531	0.9352	0.0114
SBA-Net	ISPRS'22	0.8164	0.7984	0.7104	0.9382	0.9235	0.8704	0.8612	0.0142	0.8373	0.8246	0.8159	0.9394	0.9205	0.9286	0.8618	0.0264
HFANet	TGRS'22	0.8950	0.8805	0.8651	0.9682	0.9608	0.9461	0.9298	0.0127	0.9059	0.8917	0.8697	0.9727	0.9662	0.9467	0.9355	0.0116
ESGNet	TCSVT'23	0.8907	0.8754	0.8634	0.9781	0.9732	0.9462	0.9374	0.0051	0.9220	0.9113	0.9076	0.9858	0.9814	0.9661	0.9484	0.0065
ACCoNet	TCYB'23	0.8822	0.8464	0.7787	0.9759	0.9659	0.9381	0.9303	0.0067	0.9149	0.8952	0.8830	0.9819	0.9775	0.9770	0.9428	0.0087
BSCGNet	TGRS'23	0.8809	0.8666	0.8506	0.9693	0.9650	0.9644	0.9296	0.0079	0.9101	0.8977	0.8897	0.9784	0.9744	0.9773	0.9411	0.0093
SFANet	TGRS'24	0.8834	0.8682	0.8495	0.9770	0.9725	0.9682	0.9351	0.0058	0.9192	0.9063	0.8984	0.9830	0.9789	0.9800	0.9453	0.0077
RAGRNet	TGRS'24	0.8853	0.8771	0.8646	0.9785	0.9736	0.9761	0.9364	0.0057	0.9242	0.9157	0.9104	0.9861	0.9817	0.9835	0.9507	0.0066
UDCNet	TGRS'24	0.8821	0.8517	0.8214	0.9775	0.9689	0.9551	0.9311	0.0056	0.9239	0.9068	0.8932	0.9850	0.9803	0.9770	0.9497	0.0068
SOLNet	TGRS'24	0.8609	0.8514	0.8394	0.9624	0.9576	0.9607	0.9171	0.0078	0.9012	0.8946	0.8925	0.9734	0.9688	0.9728	0.9284	0.0111
LiteSalNet	TGRS'25	0.8878	0.8810	0.8798	0.9743	0.9633	0.9729	0.9276	0.0063	0.9124	0.9061	0.9056	0.9789	0.9699	0.9752	0.9372	0.0090
LGIPNet	TGRS'25	0.8837	0.8702	0.8563	0.9761	0.9711	0.9701	0.9339	0.0065	0.9149	0.9027	0.8924	0.9806	0.9758	0.9755	0.9450	0.0082
DPU-Former	IJCAI'25	0.8931	0.8758	0.8464	0.9816	0.9749	0.9665	0.9402	0.0056	0.9263	0.9142	0.9024	0.9868	0.9827	0.9838	0.9412	0.0062
Ours	—	0.9032	0.8876	0.8719	0.9801	0.9748	0.9457	0.9487	0.0049	0.9356	0.9243	0.9196	0.9861	0.9819	0.9650	0.9590	0.0056

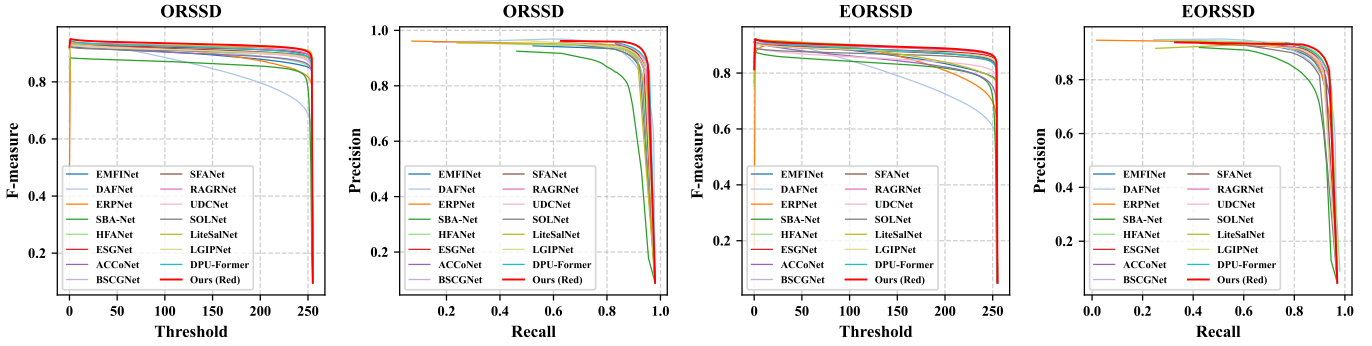


Fig. 5: The quantitative comparisons between our method and other ORSI-SOD approaches on the ORSSD [29] and EORSSD [30] datasets are presented.

effectiveness of each component in our model. The specific results are shown in Table II.

In the table, w/o DS-HGAM indicates that the difference-similarity guided hierarchical graph attention module is removed, meaning that encoder features are directly passed to the decoder via skip connections. w/o MCAEM denotes the removal of the multi-granularity collaborative attention enhancement module. w/o LESS2D indicates that the proposed locally enhanced 2D selective scan is not used in the decoder stage, and the conventional VMamba scanning strategy is adopted instead.

Our ablation study shows that the complete model achieves outstanding performance on both datasets. Specifically, it obtains scores of 0.9032, 0.9810, 0.9487, and 0.0049 on the four key metrics F_{β}^{max} , E_{ξ}^{max} , S_{α} , and MAE for the EORSSD dataset, and 0.9356, 0.9861, 0.9590, and 0.0056 for the ORSSD dataset. In contrast, the other variants exhibit varying degrees of performance degradation across these metrics. These results clearly demonstrate the effectiveness

of our proposed modules. The experimental results of w/o DS-HGAM indicate that with the introduction of the DS-HGAM module, all metrics showed improvements. On the EORSSD dataset, metrics F_{β}^{max} , E_{ξ}^{max} , and S_{α} increased by 1.25%, 0.53%, and 0.98%, respectively, while metric MAE decreased by 0.12%. Similarly, on the ORSSD dataset, metrics F_{β}^{max} , E_{ξ}^{max} , and S_{α} improved by 2.21%, 1.03%, and 1.74%, respectively, whereas metric MAE decreased by 0.4%. These results indicate that introducing the DS-HGAM module into the skip connections helps the model to capture cross-spatial and cross-scale feature relationships, thereby enabling more effective feature integration and improving the quality of the saliency map. In the w/o MCAEM setting, the results demonstrate that with the introduction of the MCAEM module, metric F_{β}^{max} on the EORSSD dataset increased from 0.8924 to 0.9032, achieving a performance improvement of 1.08%; metric E_{ξ}^{max} improved from 0.9752 to 0.9801, with a gain of 0.49%, this demonstrates that multi-scale convolutions and attention mechanisms can effectively extract multi-scale local



Fig. 6: The qualitative comparison between our method and six other approaches across various challenging scenarios.

features, thereby enhancing the model’s ability to represent salient regions and significantly improving the quality of mask prediction. The experimental results of w/o LESS2D demonstrate that by using the LESS2D module, metric F_{β}^{max} on the EORSSD dataset increased by 1.62%, metric E_{ξ}^{max} increased by 0.76%, and metric S_{α} increased by 0.93%. On the ORSSD dataset, metric F_{β}^{max} increased by 1.86%, metric E_{ξ}^{max} increased by 0.87%, metric S_{α} increased by 1.4%, while metric MAE decreased by 0.25%. The block-wise scanning strategy adopted by LESS2D enhances the

dependencies among local pixels, facilitates the learning of fine-grained local feature representations, and fully leverages the sequence modeling capability of Mamba. This enables the model to more effectively integrate global context with local details, resulting in more precise saliency maps.

V. CONCLUSION

In this paper, we propose a Mamba-based model for ORSI-SOD, named GCRPNet. Specifically, we design a DS-HGAM to perform interactive fusion of multi-scale features in the

TABLE II: The effectiveness of each component in GCRPNet. In the tables, \uparrow and \downarrow indicate that higher and lower values are preferred, respectively.

Methods	EORSSD				ORSSD			
	$F_{\beta}^{max} \uparrow$	$E_{\xi}^{max} \uparrow$	$S_{\alpha} \uparrow$	$MAE \downarrow$	$F_{\beta}^{max} \uparrow$	$E_{\xi}^{max} \uparrow$	$S_{\alpha} \uparrow$	$MAE \downarrow$
w/o DS-HGAM	0.8907	0.9748	0.9389	0.0061	0.9135	0.9758	0.9416	0.0096
w/o MCAEM	0.8924	0.9752	0.9411	0.0055	0.9214	0.9835	0.9562	0.0059
w/o LESS2D	0.8870	0.9725	0.9394	0.0055	0.9170	0.9774	0.9450	0.0081
Ours	0.9032	0.9801	0.9487	0.0049	0.9356	0.9861	0.9590	0.0056

skip connections. By leveraging graph neural networks, DS-HGAM enables modeling of cross-spatial relationships to integrate features from different regions, thereby generating higher-quality saliency maps and enhancing the model’s robustness and generalization capability. Meanwhile, to address the limitations of existing Mamba models in local information modeling, we further propose a novel LEVSS Block and incorporate it into the decoding stage of the network. This module integrates two submodules: MCAEM and LESS2D. The MCAEM module expands the receptive field by employing depthwise separable convolutions with multiple kernel sizes and parallel attention mechanisms, enabling the model to better adapt to objects of varying scales and appearances. In addition, to further improve local modeling capability, the LESS2D module performs block-wise scanning on multi-scale feature maps, which strengthens local feature representations and effectively integrates global context modeling with local detail learning. Extensive experimental results demonstrate that the proposed model achieves state-of-the-art performance on ORSI-SOD tasks, fully validating its effectiveness and superiority.

REFERENCES

- [1] A. Borji, M.-M. Cheng, H. Jiang, and J. Li, “Salient object detection: A benchmark,” *IEEE Transactions on Image Processing*, vol. 24, no. 12, pp. 5706–5722, 2015.
- [2] R. Cong, J. Lei, H. Fu, M.-M. Cheng, W. Lin, and Q. Huang, “Review of visual saliency detection with comprehensive information,” *IEEE Transactions on Circuits and Systems for Video Technology*, vol. 29, no. 10, pp. 2941–2959, 2018.
- [3] S. Hong, T. You, S. Kwak, and B. Han, “Online tracking by learning discriminative saliency map with convolutional neural network,” in *International Conference on Machine Learning*, 2015, pp. 597–606.
- [4] W. Feng, R. Han, Q. Guo, J. Zhu, and S. Wang, “Dynamic saliency-aware regularization for correlation filter-based object tracking,” *IEEE Transactions on Image Processing*, vol. 28, no. 7, pp. 3232–3245, 2019.
- [5] S. Qiu, Y. Zhao, J. Jiao, Y. Wei, and S. Wei, “Referring image segmentation by generative adversarial learning,” *IEEE Transactions on Multimedia*, vol. 22, no. 5, pp. 1333–1344, 2019.
- [6] G. Li, Z. Liu, R. Shi, Z. Hu, W. Wei, Y. Wu, M. Huang, and H. Ling, “Personal fixations-based object segmentation with object localization and boundary preservation,” *IEEE Transactions on Image Processing*, vol. 30, pp. 1461–1475, 2020.
- [7] K. Gu, S. Wang, H. Yang, W. Lin, G. Zhai, X. Yang, and W. Zhang, “Saliency-guided quality assessment of screen content images,” *IEEE Transactions on Multimedia*, vol. 18, no. 6, pp. 1098–1110, 2016.
- [8] S. Yang, Q. Jiang, W. Lin, and Y. Wang, “Sgdnet: An end-to-end saliency-guided deep neural network for no-reference image quality assessment,” in *Proceedings of the 27th ACM International Conference on Multimedia*, 2019, pp. 1383–1391.
- [9] Z. Ai, H. Luo, and J. Wang, “A lightweight multi-stream framework for salient object detection in optical remote sensing,” *IEEE Transactions on Geoscience and Remote Sensing*, 2025.
- [10] Y. Quan, H. Xu, R. Wang, Q. Guan, and J. Zheng, “Orsi salient object detection via progressive semantic flow and uncertainty-aware refinement,” *IEEE Transactions on Geoscience and Remote Sensing*, vol. 62, pp. 1–13, 2024.
- [11] Q. Wang, Y. Liu, Z. Xiong, and Y. Yuan, “Hybrid feature aligned network for salient object detection in optical remote sensing imagery,” *IEEE Transactions on Geoscience and Remote Sensing*, vol. 60, pp. 1–15, 2022.
- [12] Q. Zhang, L. Zhang, W. Shi, and Y. Liu, “Airport extraction via complementary saliency analysis and saliency-oriented active contour model,” *IEEE Geoscience and Remote Sensing Letters*, vol. 15, no. 7, pp. 1085–1089, 2018.
- [13] L. Zhang, Y. Liu, and J. Zhang, “Saliency detection based on self-adaptive multiple feature fusion for remote sensing images,” *International Journal of Remote Sensing*, vol. 40, no. 22, pp. 8270–8297, 2019.
- [14] Z. Liu, D. Zhao, Z. Shi, and Z. Jiang, “Unsupervised saliency model with color markov chain for oil tank detection,” *Remote Sensing*, vol. 11, no. 9, p. 1089, 2019.
- [15] R. Achanta, S. Hemami, F. Estrada, and S. Susstrunk, “Frequency-tuned salient region detection,” in *2009 IEEE Conference on Computer Vision and Pattern Recognition*, 2009, pp. 1597–1604.
- [16] W. Zhu, S. Liang, Y. Wei, and J. Sun, “Saliency optimization from robust background detection,” in *Proceedings of the IEEE Conference on Computer Vision and Pattern Recognition*, 2014, pp. 2814–2821.
- [17] M.-M. Cheng, N. J. Mitra, X. Huang, P. H. Torr, and S.-M. Hu, “Global contrast based salient region detection,” *IEEE Transactions on Pattern Analysis and Machine Intelligence*, vol. 37, no. 3, pp. 569–582, 2014.
- [18] L. Gao, B. Liu, P. Fu, and M. Xu, “Adaptive spatial tokenization transformer for salient object detection in optical remote sensing images,” *IEEE Transactions on Geoscience and Remote Sensing*, vol. 61, pp. 1–15, 2023.
- [19] Z. Chen, Y. Duan, W. Wang, J. He, T. Lu, J. Dai, and Y. Qiao, “Vision transformer adapter for dense predictions,” *arXiv preprint arXiv:2205.08534*, 2022.
- [20] Y. Sun, H. Xuan, J. Yang, and L. Luo, “Glconet: Learning multi-source perception representation for camouflaged object detection,” *IEEE Transactions on Neural Networks and Learning Systems*, 2024.
- [21] R. Yan, L. Yan, G. Geng, Y. Cao, P. Zhou, and Y. Meng, “Asnet: Adaptive semantic network based on transformer-cnn for salient object detection in optical remote sensing images,” *IEEE Transactions on Geoscience and Remote Sensing*, vol. 62, pp. 1–16, 2024.
- [22] J. Zhao, Y. Jia, L. Ma, and L. Yu, “Adaptive dual-stream sparse transformer network for salient object detection in optical remote sensing images,” *IEEE Journal of Selected Topics in Applied Earth Observations and Remote Sensing*, vol. 17, pp. 5173–5192, 2024.
- [23] J. Zhu, Y. Luo, X. Zheng, H. Wang, and L. Wang, “A good student is cooperative and reliable: Cnn-transformer collaborative learning for semantic segmentation,” in *Proceedings of the IEEE/CVF International Conference on Computer Vision*, 2023, pp. 11 720–11 730.
- [24] H. Huang, Y. Huang, S. Xie, L. Lin, R. Tong, Y.-W. Chen, Y. Li, and Y. Zheng, “Combinatorial cnn-transformer learning with manifold constraints for semi-supervised medical image segmentation,” in *Proceedings of the AAAI Conference on Artificial Intelligence*, vol. 38, no. 3, 2024, pp. 2330–2338.
- [25] Y. Sun, J. Yan, J. Qian, C. Xu, J. Yang, and L. Luo, “Dual-perspective united transformer for object segmentation in optical remote sensing images,” *International Joint Conference on Artificial Intelligence*, 2025.
- [26] A. Gu and T. Dao, “Mamba: Linear-time sequence modeling with selective state spaces,” *arXiv preprint arXiv:2312.00752*, 2023.
- [27] Y. Shi, B. Xia, X. Jin, X. Wang, T. Zhao, X. Xia, X. Xiao, and W. Yang, “Vmambair: Visual state space model for image restoration,” *IEEE Transactions on Circuits and Systems for Video Technology*, 2025.

- [28] P. Veličković, G. Cucurull, A. Casanova, A. Romero, P. Liò, and Y. Bengio, "Graph Attention Networks," *International Conference on Learning Representations*, 2018.
- [29] C. Li, R. Cong, J. Hou, S. Zhang, Y. Qian, and S. Kwong, "Nested network with two-stream pyramid for salient object detection in optical remote sensing images," *IEEE Transactions on Geoscience and Remote Sensing*, vol. 57, no. 11, pp. 9156–9166, 2019.
- [30] Q. Zhang, R. Cong, C. Li, M.-M. Cheng, Y. Fang, X. Cao, Y. Zhao, and S. Kwong, "Dense attention fluid network for salient object detection in optical remote sensing images," *IEEE Transactions on Image Processing*, vol. 30, pp. 1305–1317, 2020.
- [31] W. Wang, Q. Lai, H. Fu, J. Shen, H. Ling, and R. Yang, "Salient object detection in the deep learning era: An in-depth survey," *IEEE Transactions on Pattern Analysis and Machine Intelligence*, vol. 44, no. 6, pp. 3239–3259, 2021.
- [32] G. Li and Y. Yu, "Visual saliency based on multiscale deep features," in *Proceedings of the IEEE Conference on Computer Vision and Pattern Recognition*, 2015, pp. 5455–5463.
- [33] H. Sun, Y. Bian, N. Liu, and H. Zhou, "Multi-scale edge-based u-shape network for salient object detection," in *PRICAI 2021: Trends in Artificial Intelligence, PRICAI 2021, Hanoi, Vietnam, November 8–12, 2021, Proceedings, Part II 18*. Springer, 2021, pp. 501–514.
- [34] J.-X. Zhao, J.-J. Liu, D.-P. Fan, Y. Cao, J. Yang, and M.-M. Cheng, "Egnet: Edge guidance network for salient object detection," in *Proceedings of the IEEE/CVF International Conference on Computer Vision*, 2019, pp. 8779–8788.
- [35] N. Liu, N. Zhang, K. Wan, L. Shao, and J. Han, "Visual saliency transformer," in *Proceedings of the IEEE/CVF International Conference on Computer Vision*, 2021, pp. 4722–4732.
- [36] J. Zhang, J. Xie, N. Barnes, and P. Li, "Learning generative vision transformer with energy-based latent space for saliency prediction," *Advances in Neural Information Processing Systems*, vol. 34, pp. 15 448–15 463, 2021.
- [37] Z. Liu, Y. Wang, Z. Tu, Y. Xiao, and B. Tang, "Tritransnet: Rgb-d salient object detection with a triplet transformer embedding network," in *Proceedings of the 29th ACM International Conference on Multimedia*, 2021, pp. 4481–4490.
- [38] Y. Zhan, Z. Zeng, H. Liu, X. Tan, and Y. Tian, "Mambasod: Dual mamba-driven cross-modal fusion network for rgb-d salient object detection," *Neurocomputing*, vol. 631, p. 129718, 2025.
- [39] J. He, K. Fu, X. Liu, and Q. Zhao, "Samba: A unified mamba-based framework for general salient object detection," in *Proceedings of the IEEE Conference on Computer Vision and Pattern Recognition*, 2025, pp. 25 314–25 324.
- [40] G. Li, Z. Liu, D. Zeng, W. Lin, and H. Ling, "Adjacent context coordination network for salient object detection in optical remote sensing images," *IEEE Transactions on Cybernetics*, vol. 53, no. 1, pp. 526–538, 2022.
- [41] K. Huang, N. Li, J. Huang, and C. Tian, "Exploiting memory-based cross-image contexts for salient object detection in optical remote sensing images," *IEEE Transactions on Geoscience and Remote Sensing*, 2024.
- [42] P. Dong, B. Wang, R. Cong, H.-H. Sun, and C. Li, "Transformer with large convolution kernel decoder network for salient object detection in optical remote sensing images," *Computer Vision and Image Understanding*, vol. 240, p. 103917, 2024.
- [43] G. Li, Z. Bai, Z. Liu, X. Zhang, and H. Ling, "Salient object detection in optical remote sensing images driven by transformer," *IEEE Transactions on Image Processing*, vol. 32, pp. 5257–5269, 2023.
- [44] A. Gu, I. Johnson, K. Goel, K. Saab, T. Dao, A. Rudra, and C. Ré, "Combining recurrent, convolutional, and continuous-time models with linear state space layers," *Advances in Neural Information Processing Systems*, vol. 34, pp. 572–585, 2021.
- [45] J. T. Smith, A. Warrington, and S. W. Linderman, "Simplified state space layers for sequence modeling," *arXiv preprint arXiv:2208.04933*, 2022.
- [46] Y. Liu, Y. Tian, Y. Zhao, H. Yu, L. Xie, Y. Wang, Q. Ye, J. Jiao, and Y. Liu, "Vmamba: Visual state space model," *Advances in Neural Information Processing Systems*, vol. 37, pp. 103 031–103 063, 2024.
- [47] X. Liu, C. Zhang, and L. Zhang, "Vision mamba: A comprehensive survey and taxonomy. arxiv 2024," *arXiv preprint arXiv:2405.04404*.
- [48] R. Xu, S. Yang, Y. Wang, Y. Cai, B. Du, and H. Chen, "Visual mamba: A survey and new outlooks," *arXiv preprint arXiv:2404.18861*, 2024.
- [49] C. Yang, Z. Chen, M. Espinosa, L. Ericsson, Z. Wang, J. Liu, and E. J. Crowley, "Plainmamba: Improving non-hierarchical mamba in visual recognition," *arXiv preprint arXiv:2403.17695*, 2024.
- [50] H. He, Y. Bai, J. Zhang, Q. He, H. Chen, Z. Gan, C. Wang, X. Li, G. Tian, and L. Xie, "Mambaad: Exploring state space models for multi-class unsupervised anomaly detection," *arXiv preprint arXiv:2404.06564*, 2024.
- [51] T. Huang, X. Pei, S. You, F. Wang, C. Qian, and C. Xu, "Localmamba: Visual state space model with windowed selective scan," in *European Conference on Computer Vision*, 2024, pp. 12–22.
- [52] A. Gu, K. Goel, and C. Ré, "Efficiently modeling long sequences with structured state spaces," *arXiv preprint arXiv:2111.00396*, 2021.
- [53] F. Chollet, "Xception: Deep learning with depthwise separable convolutions," in *Proceedings of the IEEE Conference on Computer Vision and Pattern Recognition*, 2017, pp. 1251–1258.
- [54] X. Zhou, K. Shen, Z. Liu, C. Gong, J. Zhang, and C. Yan, "Edge-aware multiscale feature integration network for salient object detection in optical remote sensing images," *IEEE Transactions on Geoscience and Remote Sensing*, vol. 60, pp. 1–15, 2022.
- [55] X. Zhou, K. Shen, L. Weng, R. Cong, B. Zheng, J. Zhang, and C. Yan, "Edge-guided recurrent positioning network for salient object detection in optical remote sensing images," *IEEE Transactions on Cybernetics*, vol. 53, no. 1, pp. 539–552, 2023.
- [56] Z. Huang, T.-Z. Xiang, H.-X. Chen, and H. Dai, "Scribble-based boundary-aware network for weakly supervised salient object detection in remote sensing images," *ISPRS Journal of Photogrammetry and Remote Sensing*, vol. 191, pp. 290–301, 2022.
- [57] A. Gong, J. Nie, C. Niu, Y. Yu, J. Li, and L. Guo, "Edge and skeleton guidance network for salient object detection in optical remote sensing images," *IEEE Transactions on Circuits and Systems for Video Technology*, vol. 33, no. 12, pp. 7109–7120, 2023.
- [58] D. Feng, H. Chen, S. Liu, Z. Liao, X. Shen, Y. Xie, and J. Zhu, "Boundary-semantic collaborative guidance network with dual-stream feedback mechanism for salient object detection in optical remote sensing imagery," *IEEE Transactions on Geoscience and Remote Sensing*, vol. 61, pp. 1–17, 2023.
- [59] J. Zhao, Y. Jia, L. Ma, and L. Yu, "Recurrent adaptive graph reasoning network with region and boundary interaction for salient object detection in optical remote sensing images," *IEEE Transactions on Geoscience and Remote Sensing*, 2024.
- [60] Y. Sun, J. Yang, and L. Luo, "United domain cognition network for salient object detection in optical remote sensing images," *IEEE Transactions on Geoscience and Remote Sensing*, vol. 62, pp. 1–14, 2024.
- [61] Z. Li, Y. Miao, X. Li, W. Li, J. Cao, Q. Hao, D. Li, and Y. Sheng, "Speed-oriented lightweight salient object detection in optical remote sensing images," *IEEE Transactions on Geoscience and Remote Sensing*, 2024.
- [62] L. Sun, H. Liu, X. Wang, Y. Zheng, Q. Chen, Z. Wu, and L. Fu, "Local-global information perception network for salient object detection in optical remote sensing images," *IEEE Transactions on Geoscience and Remote Sensing*, vol. 63, pp. 1–18, 2025.